3-D Reconstruction of Flame Temperature Distribution Using Tomographic and Two-Color Pyrometric Techniques

Zhong Zhou, *Member, IEEE*, Delei Tian, Zhaohui Wu, Zhiyi Bian, and Wei Wu

***Abstract*— Two-color pyrometric methods have been widely used in noncontact temperature measurement area. However, it is difficult to get synchronous monochromatic images for two-color pyrometric formula. Some researches use beam splitter to obtain two or more optical paths to capture the different monochromatic images, but the complex optical paths will bring spatiotemporal matching errors. Another method uses color camera to capture the Red, Green, Blue (RGB) channel images as the RGB monochromatic images, but substituting the Dirac delta function for spectral response function will result in the inaccuracy of the measurement results. In fact, the RGB monochromatic images can be obtained from the color image if the irradiance attenuations from color channel to single wavelength are calibrated. In this paper, a novel 3-D reconstruction method is proposed to measure the temperature distribution of combustion flame. First, the irradiance attenuations are calibrated to calculate the synchronous monochromatic images at *R* and *G* wavelengths. Second, the tomographic reconstruction of flame monochromatic emissive power is improved with visual hull restriction so that the energy distribution is more reasonable. Finally, the 3-D temperature distribution is calculated from the reconstructed monochromatic emissive power fields at *R* and *G* wavelengths using two-color pyrometric method. The alcohol and butane flames are tested in the laboratory-scale test rig. The experimental results indicate that our approach performs well in flame temperature field reconstruction.**

***Index Terms*— 3-D reconstruction, flame temperature distribution, monochromatic irradiance, temperature field measurement, two-color pyrometry.**

NOMENCLATURE

T	Temperature (K).
λ	Wavelength (nm).
C_1	First radiation constant.
C_2	Second radiation constant.
ε_λ	Monochromatic emissivity.
$M(\lambda, T)$	Monochromatic emissive power.
$E(\lambda, T)$	Monochromatic irradiance.
$2a//f^{'}$	Relative aperture.
S_λ	Spectral response for sensor.
$K_T(\lambda)$	Transmittance for optical system.
p_{ij}	Pixel value.
E_c	Irradiance for camera color channel.
E_λ	Irradiance for single wavelength.
α	Irradiance attenuation.
F_{ij}	View factor.
τ	Extinction coefficient.

Manuscript received December 1, 2014; revised April 8, 2015; accepted April 27, 2015. Date of publication July 9, 2015; date of current version October 7, 2015. This work was supported in part by the National 863 Program of China under Grant 2012AA011803 and in part by the National Natural Science Foundation of China under Grant 61472020. The Associate Editor coordinating the review process was Dr. Yong Yan. *(Corresponding authors: Zhaohui Wu and Zhong Zhou.)*

The authors are with the State Key Laboratory of Virtual Reality Technology and Systems, Beihang University, Beijing 100191, China (e-mail: wzh0005@gmail.com; zz@buaa.edu.cn).

Color versions of one or more of the figures in this paper are available online at http://ieeexplore.ieee.org.

Digital Object Identifier 10.1109/TIM.2015.2444251

I. INTRODUCTION

ACCURATE reliable measurements of 3-D flame temperature distributions are highly desirable to achieve in-depth understanding of combustion and pollutant formation processes. Due to the thermal and dynamic nature of the flame, an effective means for the spatial and temporal measurement of the flame temperature remains a challenge for combustion and measurement researchers.

A number of techniques for the measurement of flame temperature have been developed in the past. Contact measurement methods using physical probes, such as thermocouple, resistance thermometers, and gas-filled probes, are easy to implement, but suffer from obvious disadvantages including intrusive sensing, sluggish response, and single-point measurement. Laser-based optical methods, such as laser-induced fluorescence and laser scattering of molecules, capture the temperature distributions fast and accurately. However, they are unsuitable for routine operation in industrial applications due to the complication of the measurement principles and system structures. Acoustic thermometry is based on the fact that sound transfers with different speeds in different media. This method is beneficial to capture the temperature distribution in a relatively larger space, but get rather low spatial resolution results. Due to the simple system setup, high spatial resolution, fast system response, and relative low cost, optical radiation pyrometry has become a practical method to measure the 3-D temperature of luminous flames.

Optical radiation pyrometry builds the relationship between the image pixels and flame temperatures based on Planck's radiation law, which can be divided into monochromatic thermometry, two-color method, and three-color method. Zhou *et al.* [1] measure the temperature of combustion flame in the boiler through monochromatic images based on the reference temperatures. Zhou *et al.* [2] present an optical sectioning method to reconstruct the original luminosity

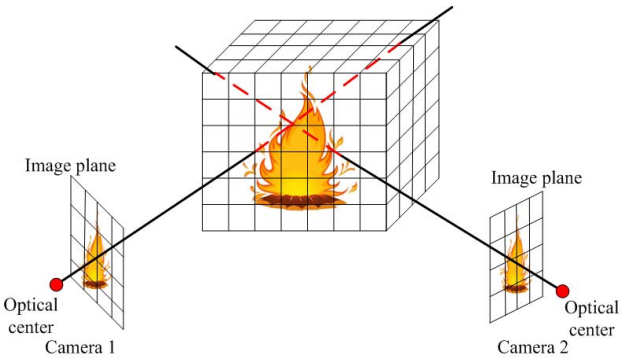

Fig. 1. Schematic of flame imaging process. The irradiance of pixel can be described as the integral of the emissive power from flame along the ray through the pixel.

and temperature distributions of steady-state candlelight. Gong *et al.* [3] further combine the optical sectioning tomography with two-color method to reconstruct the 3-D temperature distribution of the gasifier. Huang and Yan [4] introduce a beam-spilt optical system to concurrently capture the images of a flame at two different wavelengths using a single monochromatic charge-coupled device (CCD) camera and two narrow bandpass filters. Then, the transient 2-D temperature is determined from the ratio of gray levels of corresponding pixels within the two images based on the two-color principle. Lu *et al.* [5], Han *et al.* [6], and Jiang *et al.* [7] focus on the 2-D reconstruction of not only the temperature but also the soot concentration of diffusion flame, where the optical transmission and filtering assembly provided two optical paths to meet the requirement in the two-color method. Brisley *et al.* [8] address a 3-D reconstruction method to first reconstruct band-limited grayscale representations of the flame and then to determine its temperature distribution. But the method is not a true 3-D method because the reconstruction process assumes that the flame structure is rotational symmetry. Hossain *et al.* [9] investigate an optical fiber imaging-based tomographic system for the 3-D visualization of burner flame luminosity. Eight imaging fiber bundles coupled with two RGB CCD cameras are used to simultaneously acquire flame images from eight different directions around the burner. They further develop this system [10], [11] to reconstruct the laboratory-scale 3-D flame temperature and emissivity distributions using the reconstructed gray-level intensities of the red and green components and two-color pyrometric technique. This is a true 3-D reconstruction method. Zhao *et al.* [12] adopt three-color method to calculate the 2-D temperature distribution of combustion flames based on high dynamic range imaging. Fu *et al.* [13] describe a multicolor pyrometry system, respectively, based on an optical fiber spectrometer and a color CCD to measure the diesel flame temperatures.

Combining optical tomography with two-color pyrometry has obvious advantages to reconstruct the 3-D flame temperature distributions. However, getting synchronous two monochromatic images for two-color pyrometric formula is not easy. The methods using beam splitter [4]–[8], [12], [13] provide two or more optical paths for capturing two or more monochromatic images synchronously, but the complex optical paths will bring spatiotemporal matching errors. The methods using color camera [9]–[11], [13] are flexible to capture multichannel flame images, but substituting the Dirac delta function for spectral response function results in the inaccuracy of the measurement results.

The motivation of this paper is inspired by the observation that the irradiance of a specific wavelength can be obtained from the RGB images if the irradiance attenuation from RGB channels to RGB wavelengths has been measured. The camera response functions and spectrum attenuations are calibrated using spectrophotometer and optical filters to get the monochromatic irradiance images from the captured color flame images. Then, the monochromatic emissive power and temperature distributions are reconstructed using the improved optical tomographic and two-color pyrometric methods. Different flame scenes are tested to verify the efficiency of our imaging system and reconstruction approach.

II. Overview

There is a relationship between the temperature and the pixel value of flame image. According to Planck's radiation law [14], the monochromatic emissive power M of a radiation object with temperature T(K) can be described as

$$M(\lambda, T) = \varepsilon_\lambda \cdot M_b(\lambda, T) = \varepsilon_\lambda \cdot \frac{C_1 \lambda^{-5}}{e^{C_2/\lambda T} - 1} \tag{1}$$

where C_1 and C_2 are known as the Planck constants, $M_b(\lambda, T)$ is the monochromatic emissive power of the blackbody, and ε_λ is the monochromatic emissivity. In this paper, we assume that the soot particles in flame are homogeneous, optically thin, and small relative to the used wavelength, and the spectral emissivity is inversely proportional to the wavelength, i.e., $\varepsilon_\lambda \propto 1/\lambda$ [8], [15], [16]. For an image sensor (CCD or CMOS), the irradiance provokes photoelectric conversion that generates an image. In paraxial geometrical optics, the irradiance E that the image plane receives can be described as [12]

$$E(\lambda, T) = \frac{\varepsilon_\lambda K_T(\lambda) M_b(\lambda, T)}{4} \left(\frac{2a}{f'}\right)^2 \tag{2}$$

where $K_T(\lambda)$ is the optical system's transmittance and $2a/f'$ is the relative aperture. Considering the image sensor's spectral characteristics, we multiply (2) with the sensor's spectral response S_λ to get the actual irradiance [12]

$$E(\lambda, T) = \frac{\varepsilon_\lambda K_T(\lambda) M(\lambda, T) S_\lambda}{4} \left(\frac{2a}{f'}\right)^2. \tag{3}$$

In an optical imaging system, there exists a response function f to convert the amount of exposure into corresponding pixel values (p_{ij}) [12]

$$p_{ij} = f(E \cdot \Delta t) = f\left(\varepsilon_\lambda \frac{K_T(\lambda) M(\lambda, T) S_\lambda}{4} \left(\frac{2a}{f'}\right)^2 \cdot \Delta t\right). \tag{4}$$

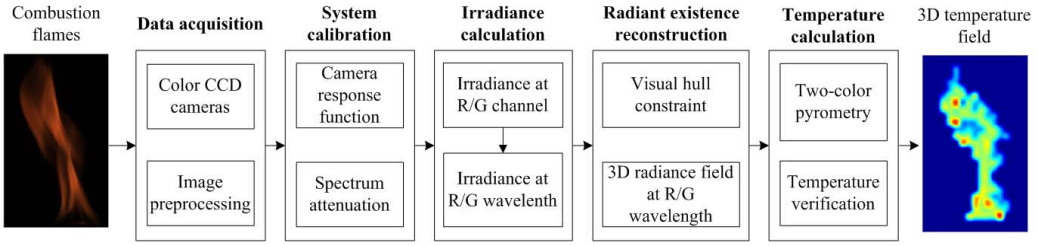

Fig. 2. Framework of our method.

Based on the relationship between pixel intensity and radiator temperature, the 3-D temperature distribution of flame can be calculated from the captured multiview images. The imaging process of the flame is shown in Fig. 1. For a pixel point in flame image, its irradiance can be expressed as the integral of the emissive power from luminous flame with different temperatures along the ray through the pixel.

Instead of using pixel intensity directly, the corresponding irradiances at different wavelengths are used to establish the relationship between the 2-D monochromatic irradiance images and 3-D monochromatic emissive power field. The reconstruction of 3-D monochromatic emissive power field from multiview irradiance images can be considered as a computer tomography problem. We divide the 3-D space into voxels, and each voxel has only a temperature. Assume that the irradiance of the ith pixel is E_i, and the monochromatic emissive power of the jth voxel is M_j, $i \in [1, M]$, $j \in [1, N]$, where M is the total number of pixels in the captured images and N is the total number of voxels of the 3-D flame. Then, the relationship between E_i and M_j can be formulated as

$$E_i = \sum_j w_{ij} M_j \tag{5}$$

where w_{ij} denotes the weight of pixel i intercepted from the total energy emitted by voxel j.

In this paper, a multiview imaging system is designed to capture the flame images precisely and a novel method is proposed to reconstruct the 3-D flame temperature field. The framework is illustrated in Fig. 2.

There are four steps in our method. First, the color images of combustion flames are captured using color CCD cameras (Section II). Second, the camera response functions and spectrum attenuations are calibrated to compute the monochromatic irradiance images at R and G wavelengths from the captured color images (Section IV). Third, the 3-D monochromatic emissive power fields at R and G wavelengths are reconstructed using the tomographic reconstruction and visual hull constraint (Sections IV-A and IV-B). Finally, the 3-D temperature distribution is calculated from the reconstructed monochromatic emissive power fields at two different wavelengths based on two-color pyrometry (Section IV-C).

III. Calculation of Monochromatic Irradiance Images

In this section, the camera response functions are calculated to restore the irradiances from color images, and the spectrum irradiance attenuations are calibrated to compute the monochromatic irradiance images at R and G wavelengths.

A. Camera Response Function Calculation

Camera response function describes the relationship between pixel value and the irradiance accepted by the CCD, and then (4) can be abbreviated as

$$p_{ij} = f(E_i \cdot \Delta t_j) \tag{6}$$

where f is the camera response function, p_{ij} is the ith pixel of the jth image, Δt_j is the jth image exposure time, and E_i is the corresponding irradiance value. As long as the inverse function of f (denoted as g) exists, (6) can be rewritten as

$$g(p_{ij}) = \ln f^{-1}(p_{ij}) = \ln E_i + \ln \Delta t_j. \tag{7}$$

The irradiance value can be obtained from the corresponding pixel value if g and exposure time Δt_j are known. In this paper, we adopt the multiexposure method proposed in [19] to compute the camera response function. Let g be a smooth and monotonic function, and $p_{\min}$ and $p_{\max}$ be the least and greatest pixel values (integers). We calculate the $g(p)$ and the $\ln E_{ij}$ to minimize the following quadratic objective function:

$$O = \sum_{i=1}^{N}\sum_{j=1}^{M}\{w(p_{ij})[g(p_{ij}) - \ln E_i - \ln \Delta t_j]\}^2 + \lambda \sum_{p=p_{\min}}^{p=p_{\max}} [w(p)g^n(p)]^2 \tag{8}$$

where N is the number of pixel locations, M is the number of images, $w(p)$ is the weighting function that is used to fit the data more near the extreme pixel value, and λ controls the smoothness of g. The first term of (8) ensures the solution satisfies (7), and the second term ensures the function g is smooth. Obviously, this is a typical linear least-square problem that can be solved by such standard methods as singular value decomposition.

In fact, the solutions for the camera response function $g(p_{ij})$ and the irradiance E_j are relative values that can be regulated by a scale factor c. We use a photometer to further measure the absolute irradiance to determine the constant c. For a color camera, the response functions of R, G, and B channels are calibrated independently. The calibration results of one specific camera are shown in Fig. 3.

In Fig. 3, the red, green, and blue curves express the calculated response functions for the R, G, and B channels,

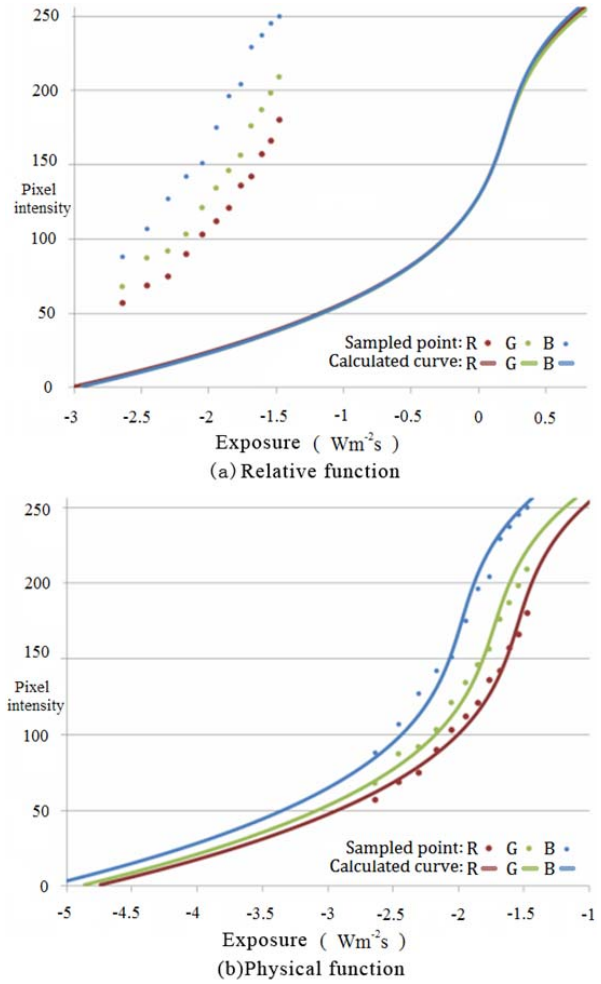

Fig. 3. Response functions of camera point-gray Flea2 08S2C for R, G, and B channels. (a) Relative response functions, where $g(p_{\text{middle}}) = 0$ [16]. (b) Physical response functions, where the constant c was determined using photometer.

respectively, and the discrete points represent the sampled response functions using color camera and photometer. It is clear that the calculated functions accord well with the sampled points [see Fig. 3(b)].

B. Irradiance Attenuation Calibration

The relationship between the pixel value and irradiance at a specific wavelength is described as

$$E_\lambda = \alpha(\lambda, \text{pixel}) \cdot E_c = \alpha \cdot g(p_{ij}) \tag{9}$$

where α is decided by wavelength λ and pixel gray level and g is the inverse of camera response function.

In this section, we calculate the irradiance attenuation (α) from the color channel (E_c) to the single wavelength (E_λ); the process is shown in Fig. 4.

There are five steps for attenuation calibration.

1) A projector is used to generate a stable light source with a given intensity, and a spectrophotometer is employed to calibrate the brightness value.
2) Capture the images of an identical scene using color camera ($I_{c\_R/G/B}$) and monochromatic camera with R, G, and B narrow-band filter ($I_{\lambda\_R/G/B}$), respectively.

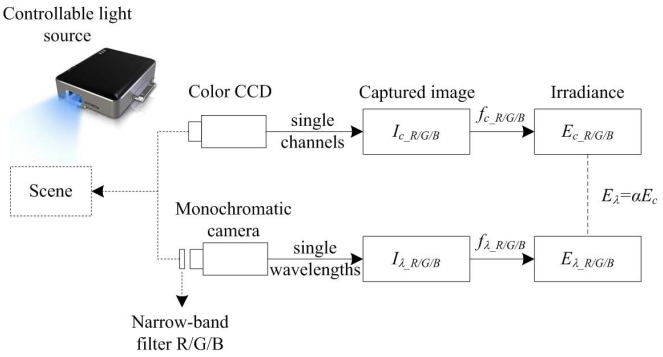

Fig. 4. Irradiance attenuation calibration from single channel to single wavelength.

3) Restore the single-channel's irradiance ($E_{c\_R/G/B}$) and the single-wavelength's irradiance ($E_{\lambda\_R/G/B}$) from I_c and I_λ based on the calibrated camera response curves [see Figs. 3(b) and 5(b)], respectively.
4) Compute the attenuation coefficient $\alpha(\lambda, \text{pixel})$ based on (9).
5) Change the intensity of light source and repeating (2)–(4).

The monochromatic images are captured by placing a narrow-band filter ($R/G/B$) between the lens and object. In this paper, the three center wavelengths of the narrow-band filters are 650, 532, and 450 nm, each with a bandwidth of 20 nm. The single-spectral camera response functions are calibrated (see Fig. 5) using the method in Section III-A. Then, the monochromatic irradiance images can be calculated from the captured monochromatic images and the camera response functions.

Therefore, the irradiance attenuations at R and G wavelengths are calibrated for our optical system, as shown in Fig. 6.

C. Monochromatic Irradiance Image Calculation and Verification

After getting the camera response functions and irradiance attenuations, we can calculate the RGB monochromatic irradiance images from the captured color image, as shown in Fig. 7.

To test our calibration method, we compare the calculated monochromatic image with captured monochromatic image (see Fig. 8). First, the color image is captured using color camera on a static scene, where the exposure time is 20 ms. Second, the monochromatic images [Fig. 8(a)] are captured using monochromatic camera for the identical scene, where the exposure time is 600 ms for red wavelength and 360 ms for green. Third, the monochromatic images at R and G wavelengths [Fig. 8(b)] are calculated from the color image based on our calibrated camera response functions and attenuation, where the exposure time also sets to 600 and 360 ms, respectively.

Fig. 8(a)–(d) shows the captured monochromatic images using monochromatic cameras directly, the reconstructed monochromatic images from captured color images using our method, the residual error of (a) and (b), and the histogram of

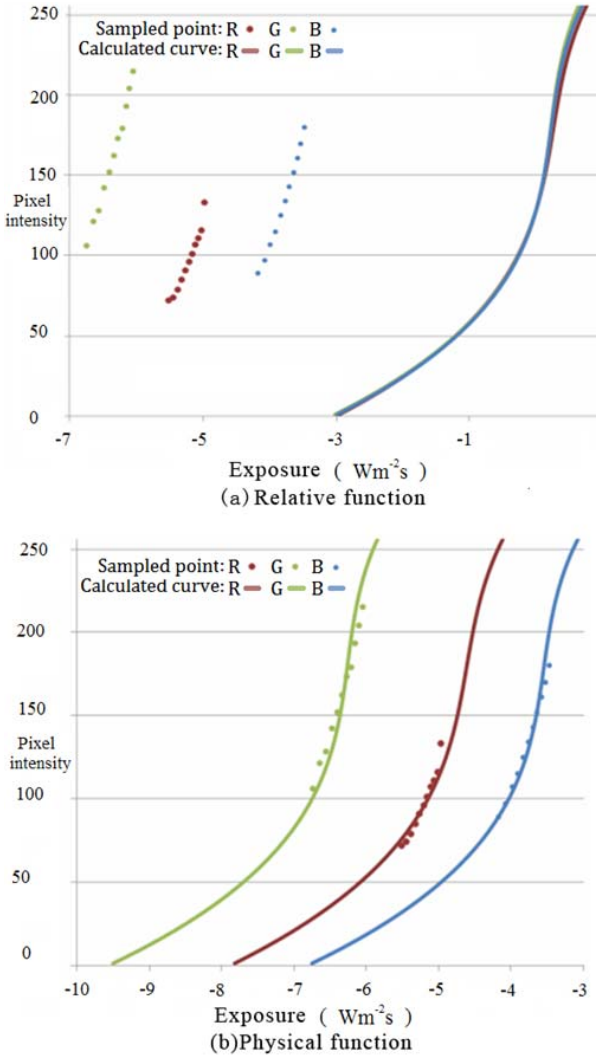

Fig. 5. Response functions of camera point-gray Flea2 08S2C for R, G, and B single wavelengths. (a) Relative response functions. (b) Physical response functions.

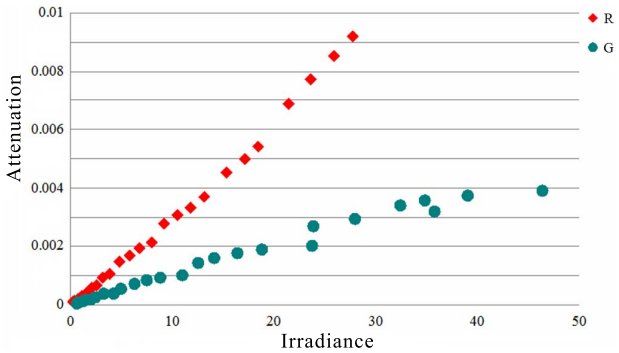

Fig. 6. Irradiance attenuation α at R and G wavelengths for our optical system.

relative error, respectively, where the abscissa is the pixel's relative difference and the vertical ordinate is the ratio of pixel number. The reconstructed monochromatic images are basically in accordance with the captured images. More than 90% pixels' reconstructed error is less than 20, as shown in Fig. 8(c) and (d). The reconstruction errors mainly come from the refraction of narrow-band filters, which can be reduced using a displacement calibration. Therefore, the calibrated camera response functions and attenuations are reliable to calculate the monochromatic irradiance images.

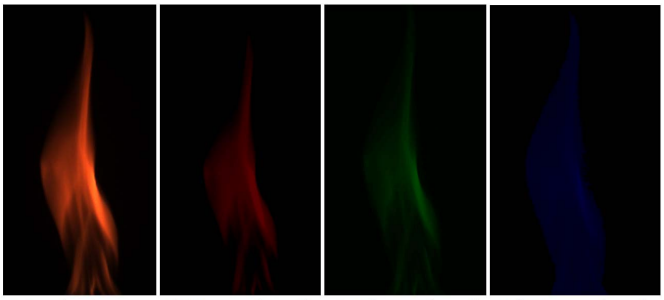

Fig. 7. Calculated monochromatic images. (a) Captured color image. (b)–(d) Calculated monochromatic (R, G, and B) images from (a).

IV. 3-D Temperature Field Reconstruction

In this section, a novel reconstruction method is proposed to rebuild 3-D flame temperature distribution. The tomographic reconstruction and visual hull techniques are employed to reconstruct the 3-D monochromatic emissive power fields at R and G wavelengths from multiview irradiance images. The reconstructed monochromatic emissive power fields are further used to calculate 3-D temperature distributions based on the two-color method.

A. Tomographic Reconstruction of Monochromatic Emissive Power Fields

Reconstructing 3-D emissive power field from multiview irradiance images can be considered as a computer tomography problem. In order to identify whether a voxel influences a specific pixel, starting from optical center O, we cast four back-projection rays that point to the four corner of the pixel, respectively. For each pixel, a square pyramid with top point O is generated. If a voxel is inside of or intersects with the pyramid, we consider that it has effect on the pixel intensity, as illustrated in Fig. 9.

The relationship between pixel's irradiance and voxel's emissive power is shown in (5). To accurately calculate the weight coefficient w_{ij}, we compute the view factor from voxel to pixel. The view factor [17], F_{ij}, is defined as the fraction intercepted from the total emitted energy. As Fig. 10 shows, we consider the voxel as a tiny ball and take the pixel as a small patch in the image plane.

In Fig. 10, L is the distance between voxel center and pixel center, R is the radius of voxel, $\overrightarrow{r_1}$ is the normal of pixel, $\overrightarrow{r_2}$ is the direction from pixel center to voxel center, and β denotes the angle between $\overrightarrow{r_1}$ and $\overrightarrow{r_2}$. Assume that the voxel ball has a diffuse surface, without scattering, then the view factor F_{ij} from voxel j to pixel i is

$$F_{ij} = \int \frac{\cos\beta_1 \cos\beta_2}{\pi R^2} dA = \frac{R^2}{L^2} \cos\beta \tag{10}$$

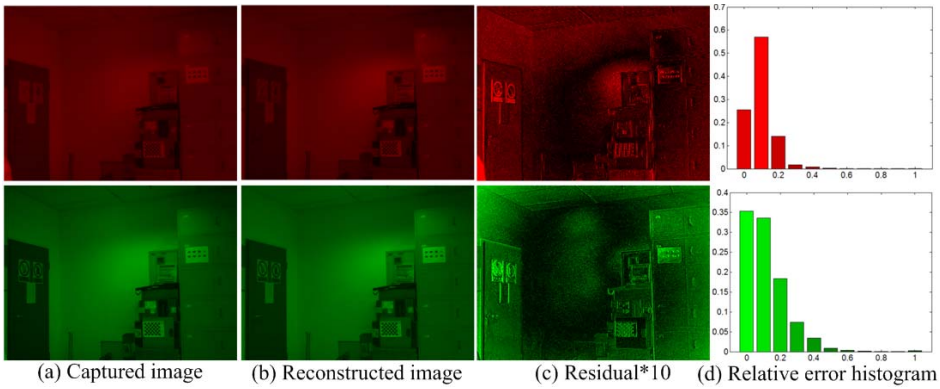

Fig. 8. Comparison between the captured monochromatic image and the reconstructed image. The wavelength of the first row is 650 nm, and the second row is 530 nm.

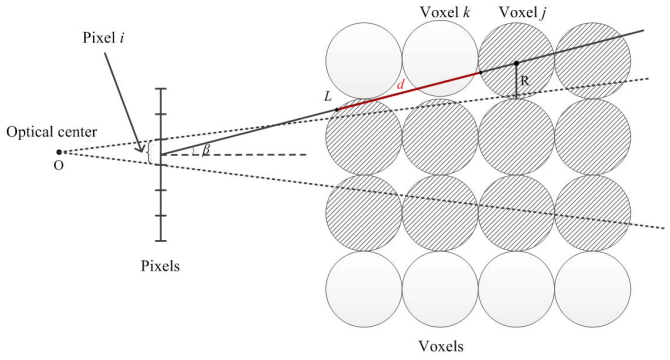

Fig. 9. Diagram of the scope in voxels for each pixel. The shaded voxels have influence on the intensity of pixel i, and the white balls do not.

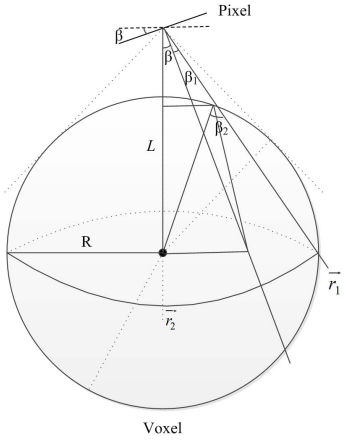

Fig. 10. Diagram of view factor calculation.

where β_1 and β_2 are as shown in Fig. 9 and dA is the surface element.

As well as view factor, the transparency τ_j is also related to the weight w_{ij}. The transparency can be thought as the degree by which the flame products between the pixel and a position x along the ray permit the radiance from further away to reach that pixel [18]. Assuming that the flame is homogeneous ($D(t) = 1$), which means that the effects of particle mass and scattering are ignored [15], then the transparency of voxel j is expressed as

$$\tau = \exp\left(-\sigma \int_0^x D(t)dt\right) = \exp\left(-\sigma \int_0^d 1dt\right) = e^{-d\sigma} \tag{11}$$

where the extinction coefficient σ is a positive constant dependent on the medium and d is the distance of light through flame before arriving in voxel j.

According to (3) and (5), the weight w_{ij} can be described as

$$w_{ij} = \frac{K_T(\lambda)}{4} \cdot \left(\frac{2a}{f'}\right)^2 \cdot \frac{\tau F_{ij}}{s_i} \cdot 4\pi R^2 = C_1 \cdot {C_2}^d \cdot \frac{\cos\beta}{L^2} \tag{12}$$

where s_i is the area of pixel i, $C_1 = (K_T(\lambda)\pi R^4/s_i) \cdot (2a/f')^2$ and $C_2 = e^{-\sigma}$. Then, the weight is decided by d, L, and β, which can be computed in preprocessing. Therefore, (5) is written as a linear system

$$W \cdot M = E \tag{13}$$

where W is the weight matrix, E is the 3-D emissive power field, and M is the irradiance vector for flame images pixels. Obviously, W is a large sparse matrix, and the linear system is an ill-conditional problem. As the nonnegative least-square problem equals to a quadratic programming (QP) problem, (13) can be described as

$$\hat{M} = \arg\min_{M \geq 0} \frac{1}{2} M^T (W^T W) M + (-W^T E) M. \tag{14}$$

Equation (14) is robustly solved using QP solver [19] in our work.

B. Visual Hull Constraint

We restrict the solution space of (14) using additional information about the visual hull to discard the variables that need not to be computed. Visual hull is a conservative approximation to the geometry of a rigid object that is found by intersecting the back-projected silhouettes from all the source images. In our work, the 3-D visual hull is computed from 2-D silhouettes of four-view images by rapid octree construction [20]. The flame voxels with possibly nonzero coefficients are guaranteed to lie inside the visual hull.

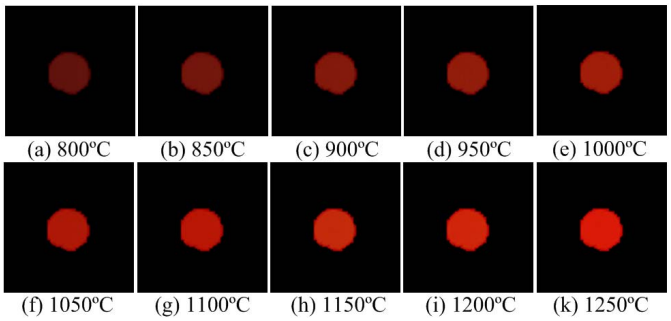

Fig. 11. RGB images of the blackbody cavity captured by our system from 800 °C to 1250 °C, where the intensity of R channel is compressed using logarithm.

C. Two-Color Method for Temperature Reconstruction

Given a voxel's monochromatic emissive power at R and G wavelengths, its temperature can be obtained based on the two-color pyrometric method [4]

$$T = \frac{C_2(1/\lambda_R - 1/\lambda_G)}{\ln \frac{M(\lambda_G,T)}{M(\lambda_R,T)} + \ln \frac{S(\lambda_R)}{S(\lambda_G)} + \ln \frac{\varepsilon(\lambda_G)}{\varepsilon(\lambda_R)} + \ln \left(\frac{\lambda_G}{\lambda_R}\right)^5} \quad (15)$$

where T is the true temperature of a voxel, C_2 is the second Planck's constant, and λ_R and λ_G are the central wavelengths corresponding to the R and G components of the CCD camera, which are 650 and 530 nm, respectively. $M(\lambda_R, T)$ and $M(\lambda_G, T)$ are the reconstructed monochromatic emissive power for wavelengths R and G. $S(\lambda_R)$ and $S(\lambda_G)$ are the spectral sensitivities of the CCD for R and G. $\varepsilon(\lambda_R)$ and $\varepsilon(\lambda_G)$ are the spectral emissivities of R and G, respectively. Normally, gray-body behavior is assumed for the flame [i.e., $\varepsilon(\lambda_R)/\varepsilon(\lambda_G) \approx 1$] as the wavelengths are very close to each other [21]. Flower [15] proved that, when assuming that the particles in flame are homogeneous, optically thin, isothermal along a horizontal line through the flame, and small relative to the used wavelength, the spectral emissivity is inversely proportional to the wavelength ($\varepsilon(\lambda_R/\varepsilon(\lambda_G)) \approx \lambda_G/\lambda_R$), then (15) is described as [8], [16]

$$T = \frac{C_2(1/\lambda_R - 1/\lambda_G)}{\ln \frac{M(\lambda_G,T)}{M(\lambda_R,T)} + \ln \frac{S(\lambda_R)}{S(\lambda_G)} + \ln \left(\frac{\lambda_G}{\lambda_R}\right)^6} \quad (16)$$

where $S(\lambda_R)/S(\lambda_G)$ is the instrument factor that is calibrated using a blackbody furnace (LumaSense M330). The blackbody furnace has a blackbody cavity with a 40-mm inner diameter and an emissivity of approximately 0.99 (300 °C–1700 °C). Fig. 11 shows the captured RGB images of the blackbody cavity from 800 °C to 1250 °C. Fig. 12 shows the calibrated relationship between the instrument factor and the gray-level ratio of the blackbody images. A quadratic polynomial function is used to fit this relationship. The fitted function is $S = 100.3(M_G/M_R)^2 - 5.28(M_G/M_R) + 4.551$, where the root-mean-square error is only 0.08316.

V. Results and Discussion

In this paper, a multicamera digital imaging system that comprises four color CCD cameras is used to acquire synchronous 2-D flame images from different directions.

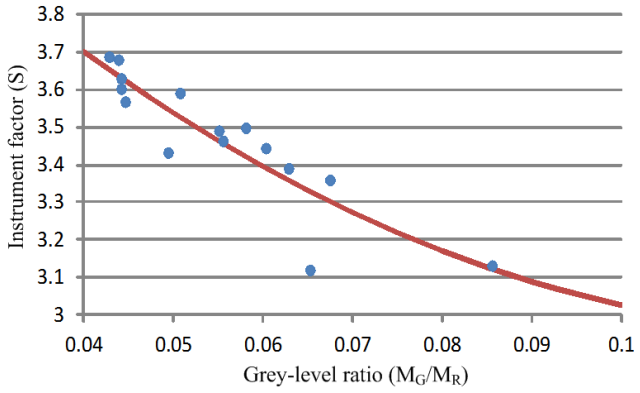

Fig. 12. Relationship between the instrument factor and gray-level ratio.

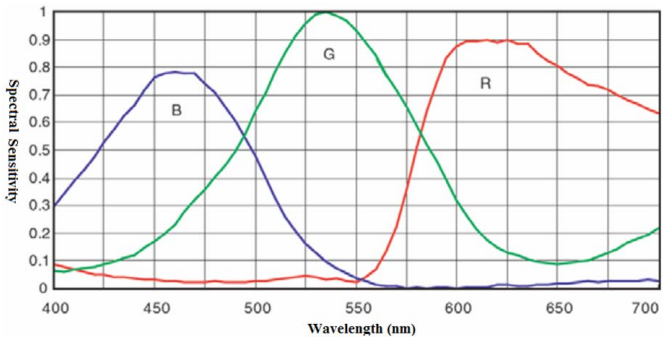

Fig. 13. Spectral response functions for the point-gray Flea2 FL2-08S2C camera.

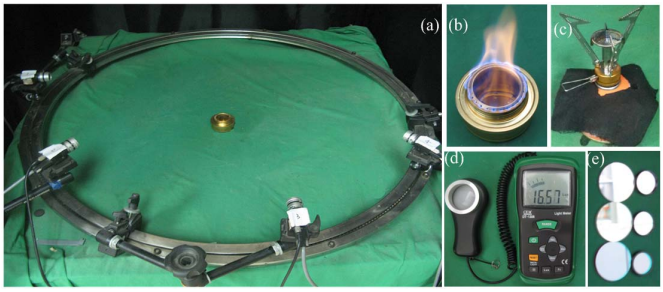

Fig. 14. Physical devices of flame image acquisition. (a) Experimental platform. (b) Target alcohol flame stove. (c) Target butane flame stove. (d) Spectrophotometer. (e) Narrow-band filters.

In our system, the integrated camera is point-gray Flea 2 series 08S2C color camera, with a frame rate of 30 frames/s at a maximum resolution of 1032 × 776. The spectral response functions of the Flea 2 camera are shown in Fig. 13, and the central wavelengths corresponding to the R, G, and B components of the camera are 650, 530, and 455 nm, respectively.

The physical devices of our system are shown in Fig. 14. In our imaging system, the cameras are located on an auxiliary ring with a 45° interval. The target flame is placed at the center of the ring, which is equidistant to each camera. Eight-pin (General Purpose Input/Output) connector is used to synchronously trigger the cameras. To avoid the influence of other light sources, the flame images are captured in a total dark environment. The extrinsic and intrinsic parameters of all the cameras are calibrated with standard techniques [22].

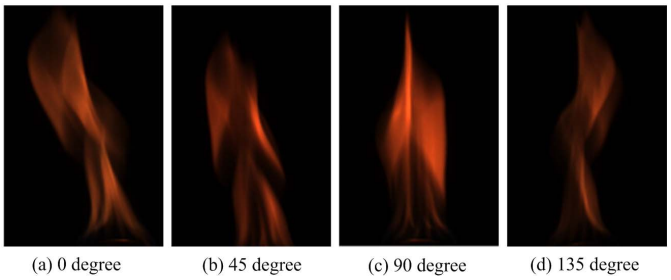

Fig. 15. Captured RGB images for combustion alcohol flame (Frame 38).

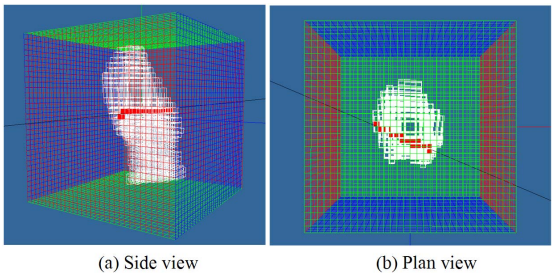

Fig. 16. Visual hull constraint. The solution space of 3-D radiance existence is restricted using visual hull to abandon the impossible zones for shape constraint.

The alcohol and butane flames were tested to verify the effectiveness of our method. An alcohol furnace with an outlet diameter of 50 mm and a butane furnace are used to generate laboratory-scale flames, respectively. The heights of the generated flames are about 150 mm. For each flame scene, we captured 100 frames of 640 × 480 images from four different directions synchronously, with a frame rate of 12 frames/s. The exposure time is 80 ms to ensure that the pixels are not saturated in any spectral channel for flames, and a frame of the captured alcohol flame images is shown in Fig. 15. It is obvious that there are no saturated pixels in the captured flame images.

Fig. 16 shows the generated visual hull from the 2-D silhouettes of four-view images of Fig. 15. The white cubes are the voxels of the visual hull, and the black line is the ray emitted from the center pixel of the 0° image. The marked red cubes are the intersection of black line with 3-D flame, and only the red voxels have contribution to the center pixel. The resolution of the 3-D voxel space is 32^3, but the number of voxels in visual hull is less than 2000. The physical resolution of each voxel is $(0.44375\ \text{cm})^3$. Therefore, the solution space of (5) was restrained from 32 768 to less than 2000. In Fig. 16, the dimensions of weight matrix w_{ij} are 69 131 × 1990, where 69 131 is the number of pixels for four inputted flame images and 1990 is the number of voxels inside the visual hull. Therefore, the visual hull is effective to restrict the solution space of tomographic reconstruction.

Fig. 17 shows the cross-sectional distribution of the reconstructed temperature field. Fig. 17(a)–(c) shows the captured flame image at 0°, where the white lines indicate the different positions of the cross sections, stereoscopic view of the temperature distributions for each cross section, and the temperature distribution of a cross section, respectively.

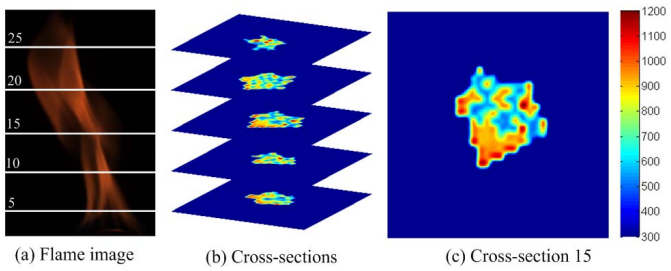

Fig. 17. Visualization of the temperature distribution of cross sections for Frame 38, alcohol flame.

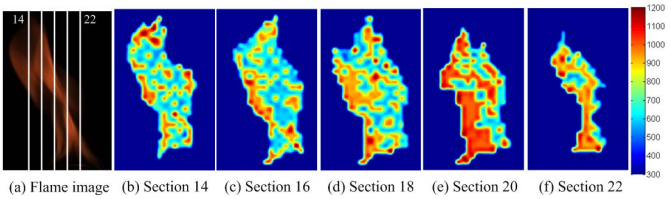

Fig. 18. Visualization of the temperature distribution of longitudinal sections for Frame 38, alcohol flame.

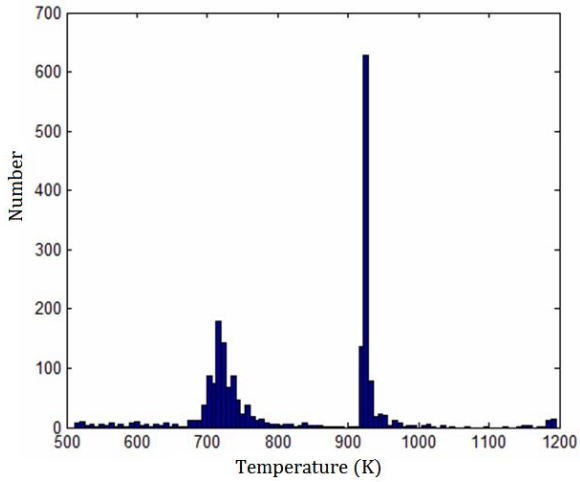

Fig. 19. Histogram of the reconstructed temperature field for Frame 38, alcohol flame.

In Section 15, the maximum temperature is 1191 K, the minimum temperature is 519 K, and the average temperature is about 814 K.

Fig. 18 further shows the longitudinal-section distribution of the reconstructed temperature field. The longitudinal sections are generated along the central axis of viewpoint 0. Section 14 is the nearest longitudinal section to viewpoint 0, Section 22 is the farthest one, and Section 16 is the middle plane of 3-D flame. In Section 16, the maximum temperature is 1194 K, the minimum temperature is 531 K, and the average temperature is about 808 K. In terms of the whole temperature field, the maximum temperature is 1195 K, the minimum temperature is 512 K, and the average temperature is about 794 K. The histogram of the reconstructed temperature distribution for Frame 38 is shown in Fig. 19. From Fig. 19, only a small percentage of the temperatures less than 700 K can be observed. These lower temperatures may be caused by the fact that the visual hull is greater than the flame body.

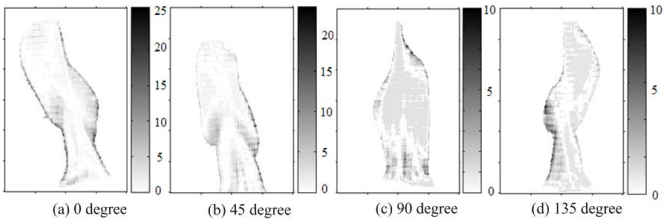

Fig. 20. Visualizing the reproject irradiance error.

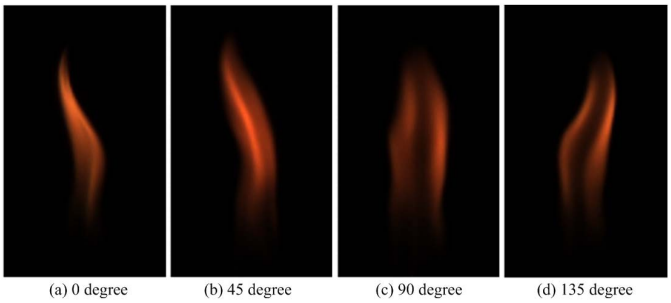

Fig. 21. Captured RGB images for combustion butane flame (Frame 8).

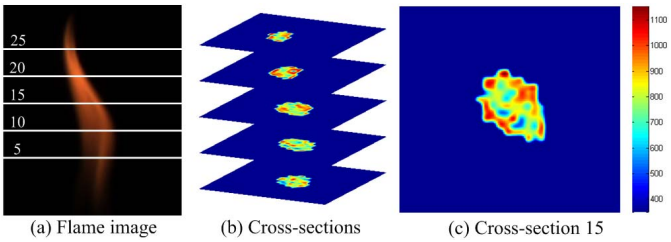

Fig. 22. Visualization of the temperature distribution of cross sections for Frame 8, butane flame.

Fig. 20 shows the reproject irradiance errors for the reconstructed temperature fields. The gray level of the image denotes the difference between the captured irradiance image and the back-projected irradiance image from the reconstructed temperature field. The reconstructed errors are mainly concentrated on the boundary portion; this is because the boundary contains more background information. The maximum error is less than 20%, which is accepted in dynamic flame reconstruction.

We further tested the butane flames in this paper. The eighth frame of the captured butane flames is shown in Fig. 21. It is obvious that there are no saturated pixels in the captured images. Fig. 22 shows the cross-sectional distribution of the reconstructed temperatures. In Section 15, the maximum temperature is 1068 K, the minimum temperature is 512 K, and the average temperature is about 824 K. Fig. 23 shows the longitudinal-section distribution of the reconstructed temperature field. In Section 18, the maximum temperature is 1098 K, the minimum temperature is 504 K, and the average temperature is about 819 K. In terms of the whole temperature field, the maximum temperature is 1114 K, the minimum temperature is 502 K, and the average temperature is about 833 K. The maximum error is less than 4%. In general, the range of reconstructed flame temperatures

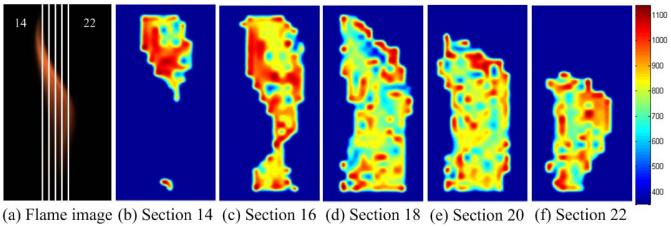

Fig. 23. Visualization of the temperature distribution of longitudinal sections for Frame 8, butane flame.

meets the empirical value of alcohol and butane flames. Our method is effective to reconstruct 3-D flame temperature fields.

There are still some limitations in our method, i.e., the resolution of voxels is only 32^3, which can be further improved; lack of straightforward and reliable verification approach for the reconstructed results; and dynamic information is lost between the adjacent reconstructed frames as the captured frame is limited.

VI. Conclusion and Future Work

In this paper, a novel tomographic method has been presented to reconstruct 3-D flame temperature distribution. First, the flame images were captured from four different views using the color CCD cameras. Second, the camera response functions and the spectrum irradiance attenuations were calibrated to restore the monochromatic irradiance images at R and G wavelengths. Third, the tomographic reconstruction and visual hull techniques were employed to reconstruct the 3-D monochromatic emissive power and temperature fields from the multiview irradiance images. An instrumentation system was presented, and a series of experiments has been carried out, the results of which are satisfactory.

Future work includes exploring the new verification approach for the reconstructed results, enriching the dynamic information between reconstructed frames based on the Navier–Stokes equations.

Acknowledgment

The authors would like to thank the team of Prof. H. Zhou at Tsinghua University for their help in our calibration using the blackbody furnace and Prof. Y. Duan of Missouri University for his help in proofreading. The authors would also like to thank the anonymous reviewers for their valuable suggestions that helped improve a lot in our revision.

References

[1] H. Zhou *et al.*, "Experimental study on image processing of flame temperature distribution in a pilot scale furnace," *Proc. Chin. Soc. Elect. Eng.*, vol. 15, no. 5, pp. 295–300, 2002.

[2] B. Zhou, J. Zhang, and S. Wang, "Reconstruction of flame temperature field with optical sectioning method," *IET Image Process.*, vol. 5, no. 5, pp. 382–393, 2011.

[3] Y. Gong, Q. Guo, Q. Liang, Z. Zhou, and G. Yu, "Three-dimensional temperature distribution of impinging flames in an opposed multiburner gasifier," *Ind. Eng. Chem. Res.*, vol. 51, no. 22, pp. 7828–7837, 2012.

[4] Y. Huang and Y. Yan, "Transient two-dimensional temperature measurement of open flames by dual-spectral image analysis," *Trans. Inst. Meas. Control*, vol. 22, no. 5, pp. 371–384, 2000.

[5] G. Lu, Y. Yan, G. Riley, and H. C. Bheemul, "Concurrent measurement of temperature and soot concentration of pulverized coal flames," *IEEE Trans. Instrum. Meas.*, vol. 51, no. 5, pp. 990–995, Oct. 2002.
[6] Y.-T. Han, K.-H. Lee, and K.-D. Min, "A study on the measurement of temperature and soot in a constant-volume chamber and a visualized diesel engine using the two-color method," *J. Mech. Sci. Technol.*, vol. 23, no. 11, pp. 3114–3123, 2009.
[7] F. Jiang, S. Liu, S. Liang, Z. Li, X. Wang, and G. Lu, "Visual flame monitoring system based on two-color method," *J. Thermal Sci.*, vol. 18, no. 3, pp. 284–288, 2009.
[8] P. M. Brisley, G. Lu, Y. Yan, and S. Cornwell, "Three-dimensional temperature measurement of combustion flames using a single monochromatic CCD camera," *IEEE Trans. Instrum. Meas.*, vol. 54, no. 4, pp. 1417–1421, Aug. 2005.
[9] M. M. Hossain, G. Lu, and Y. Yan, "Optical fiber imaging based tomographic reconstruction of burner flames," *IEEE Trans. Instrum. Meas.*, vol. 61, no. 5, pp. 1417–1425, May 2012.
[10] M. M. Hossain, G. Lu, and Y. Yan, "Three-dimensional reconstruction of flame temperature and emissivity through tomographic imaging and pyrometric measurement," in *Proc. IEEE Int. Conf. Imag. Syst. Techn. (IST)*, Jul. 2012, pp. 13–17.
[11] M. M. Hossain, G. Lu, D. Sun, and Y. Yan, "Three-dimensional reconstruction of flame temperature and emissivity distribution using optical tomographic and two-colour pyrometric techniques," *Meas. Sci. Technol.*, vol. 24, no. 7, p. 074010, 2013.
[12] H. Zhao, H. Feng, Z. Xu, and Q. Li, "Research on temperature distribution of combustion flames based on high dynamic range imaging," *Opt. Laser Technol.*, vol. 39, no. 7, pp. 1351–1359, 2007.
[13] T. Fu, Z. Wang, and X. Cheng, "Temperature measurements of diesel fuel combustion with multicolor pyrometry," *J. Heat Transf.*, vol. 132, no. 5, pp. 051602-1–051602-7, 2010.
[14] M. Planck, *The Theory of Heat Radiation*. New York, NY, USA: Dover, 1991.
[15] W. L. Flower, "Optical measurements of soot formation in premixed flames," *Combustion Sci. Technol.*, vol. 33, nos. 1–4, pp. 17–33, 1983.
[16] Y. Huang, Y. Yan, and G. Riley, "Vision-based measurement of temperature distribution in a 500-kW model furnace using the two-colour method," *Measurement*, vol. 28, no. 3, pp. 175–183, 2000.
[17] T. L. Bergman, A. S. Lavine, F. P. Incropera, and D. P. DeWitt, *Fundamentals of Heat and Mass Transfer*. New York, NY, USA: Wiley, 2011.
[18] S. W. Hasinoff and K. N. Kutulakos, "Photo-consistent reconstruction of semitransparent scenes by density-sheet decomposition," *IEEE Trans. Pattern Anal. Mach. Intell.*, vol. 29, no. 5, pp. 870–885, May 2007.
[19] [Online]. Available: http://www.gurobi.com/documentation/5.6/reference, accessed Jul. 1, 2015.
[20] R. Szeliski, "Rapid octree construction from image sequences," *CVGIP, Image Understand.*, vol. 58, no. 1, pp. 23–32, 1993.
[21] Z. Luo and H.-C. Zhou, "A combustion-monitoring system with 3-D temperature reconstruction based on flame-image processing technique," *IEEE Trans. Instrum. Meas.*, vol. 56, no. 5, pp. 1877–1882, Oct. 2007.
[22] Z. Zhang, "A flexible new technique for camera calibration," *IEEE Trans. Pattern Anal. Mach. Intell.*, vol. 22, no. 11, pp. 1330–1334, Nov. 2000.

Zhong Zhou (M'11) received the B.S. degree from Nanjing University, Nanjing, China, and the Ph.D. degree from Beihang University, Beijing, China, in 1999 and 2005, respectively.

He is currently an Associate Professor and a Ph.D. Adviser with the State Key Laboratory of Virtual Reality Technology and Systems, Beihang University. His current research interests include augmented virtual environment, natural phenomena simulation, distributed virtual environment, and Internet-based VR technologies.

Prof. Zhou is a member of the Association for Computing Machinery and the China Computer Federation.

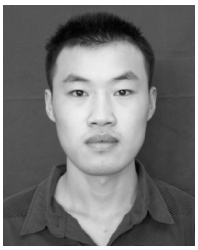

Delei Tian received the B.S. degree from Shandong University, Jinan, China, in 2012, and the M.S. degree from Beihang University, Beijing, China, in 2015.

His current research interests include physics-based flame reconstruction.

Zhaohui Wu received the M.S. degree from Yanshan University, Qinhuangdao, China, in 2009, and the Ph.D. degree from Beihang University, Beijing, China, in 2015.

His current research interests include realistic fire/fame simulation, fluid simulation, flame data capture, processing, and reuse.

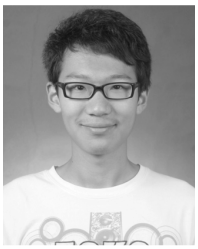

Zhiyi Bian received the B.S. degree from Beijing Jiaotong University, Beijing, China, in 2014. He is currently pursuing the M.S. degree in computer science and technology with the School of Computer Science, Beihang University, Beijing.

His current research interests include high dynamic range flame capture and reuse.

Wei Wu received the Ph.D. degree from the Harbin Institute of Technology, Harbin, China, in 1995.

He is currently a Professor with the State Key Laboratory of Virtual Reality Technology and Systems, Beihang University, Beijing, China. He is also the Chair of the Virtual Reality and Visualization Committee of the China Computer Federation. His current research interests include virtual reality, virtualization, and distributed interactive simulation.